

Retrieving the displacements of the Hutubi (China) underground gas storage during 2003–2020 from multi-track InSAR



Yuedong Wang ^{a,b}, Guangcai Feng ^{a,b,*}, Zhiwei Li ^{a,b}, Wenbin Xu ^{a,b}, Jianjun Zhu ^{a,b}, Lijia He ^{a,b}, Zhiqiang Xiong ^{a,b}, Xuejun Qiao ^c

^a School of Geosciences and Info-Physics, Central South University, Changsha 410083, China

^b Key Laboratory of Metallogenic Prediction of Nonferrous Metals and Geological Environment Monitoring Ministry of Education, Changsha 410083, China

^c Key Laboratory of Earthquake Geodesy, Institute of Seismology, China Earthquake Administration, Wuhan 430071, China

ARTICLE INFO

Editor: Jing M. Chen

Keywords:

Underground gas storage
Gas injection/extraction
Displacement
Hutubi
Time-series InSAR

ABSTRACT

Many countries and regions build underground gas storages (UGSs) to regulate the energy demand and supply in different seasons. The Hutubi underground gas storage (HUGS) in Xinjiang province is the largest UGS in China, so it is of great significance to monitor its operation. At present, the researches on the HUGS mainly rely on traditional geodetic monitoring (e.g., in-situ leveling and global navigation satellite system (GNSS)), which has a short time span and low spatial resolution. The whole-domain and long-temporal sequence surface displacements induced by gas recovery (before 2013) and injection/extraction (since 09/06/2013) were seldom reported. In this study, the large-scale background deformation was firstly obtained using the ALOS PALSAR data (2006–2011), and the displacement time series of the HUGS over 2003–2020 was observed by all available Synthetic Aperture Radar (SAR) data from multiple SAR sensors (Envisat ASAR, TerraSAR/TanDEM-X, Sentinel-1). The results show that this area had a long history of slow subsidence (2.2 mm/yr) before 2013. Since 06/2013, the surface of the HUGS showed periodic uplift and subsidence with a net uplift. The average uplift rate in the center was about 7 mm/yr during 08/2013–07/2015 and 13 mm/yr during 03/2015–05/2020. The deformation has a temporal correspondence with the gas extraction/injection process. The accuracy is assessed by the cross-validation of the results of different datasets and the GNSS measurements. The compound dislocation model (CDM) is used to model the dynamic displacements caused by gas injection/extraction in HUGS. This model can reflect the UGS volume changes and the estimated central depth (3499.7 m) and height (108.6 m) of the storage are consistent with the actual central depth (~3585 m) and height (~110 m). We also restore the dynamic change of the pore pressure and the injected gas volume during the 5–7 cycles, on the basis of the linear relations between gas injection volume, pore pressure, and CDM parameters. In 12/2017, the estimated gas inventory of the HUGS is $91.29 \times 10^8 \text{ m}^3$, about 4.7% smaller than the real gas inventory of $95.77 \times 10^8 \text{ m}^3$. At the end of the seventh injection/extraction cycle, the predicted maximum gas injection volume and pore pressure reached 11.2 billion m^3 and 36 MPa, respectively.

1. Introduction

Underground gas storage (UGS) plays an important indispensable role in global energy supply, seasonal peak shaving, and strategic reserve. The gas injection and extraction in UGS usually lead to surface displacement and have triggered seismic activities in the surrounding regions (Foulger et al., 2018; Hu et al., 2020). The scale and number of UGSs are gradually increasing in recent years (Ding and Wei, 2020). To ensure the safe operation of UGS facilities and the stable supply of

energy, it is necessary to accurately monitor the ground deformation and invert the source parameters related to this dynamic process (gas injection/extraction). The Hutubi gas field in Xinjiang province, China, has a gas extraction history of about 14 years (1998–2012). On 09/06/2013, it was transformed from a depleted reservoir to an underground gas storage, referred to as HUGS hereafter (Pang et al., 2012). HUGS is the largest UGS in China with a design capacity of 10.7 billion. Until 2020, it has been operating for more than 7 years (Jiang et al., 2020). Hence, monitoring the surface deformation and inverting the source

* Corresponding author at: School of Geosciences and Info-Physics, Central South University, Changsha 410083, China.

E-mail address: fredgps@csu.edu.cn (G. Feng).

parameters related to the gas injection/extraction process is important to understand the mechanism of the HUGS operation in this region.

Some studies have observed the surface deformation and analyzed the induced earthquakes of the HUGS by different technologies. Li et al. (2016) measured the vertical deformation at 13 stations from 2013 to 2015 by leveling technology. Qiao et al. (2018) used two continuous global navigation satellite system (GNSS) stations (2016–2017), 33 campaign sites (2013–2017), and 30 sets of descending track TerraSAR-X (2013–2015) datasets to measure the surface deformation of the HUGS. Tang et al. (2018) and Zhou et al. (2019) analyzed the earthquake triggering effects of the gas injection/extraction in HUGS using seismic wave and the UGS operation information from 2013 to 2015. Jiang et al. (2020) conducted quantitative analysis on the geomechanics of the seismicity induced by the HUGS through a two-dimensional (2-D) hydrogeologic framework on one seismic reflection profile, using the horizontal displacement information from 13 campaign GNSS stations (2013–2017) and the water well data like Qiao et al. (2018). In these studies, leveling, GNSS, and water well data were used to map the surface deformation on HUGS, but the spatial resolution and time span of these techniques are limited. Single observation geometry (descending track) InSAR dataset was also used to observe the surface deformation of HUGS, but the temporal coverage of the dataset is short (2013–2015). Therefore, current researches only focus on the deformation or geomechanics in the injection/extraction of the UGS stage (after 2013), which has a short time span, ignoring the impacts of the deformation caused by historical mining (1998–2012). Moreover, very few investigations have been done on the large-scale background deformation near the HUGS, which, however, is important for understanding the spatial-temporal features of surface deformation. Furthermore, the proposed deformation models are two dimensional (Jiang et al., 2020) or simulate the vertical deformation of some points (Qiao et al., 2018). A comprehensive understanding of the long-temporal evolution history of the deformation in the HUGS, including gas production and injection/extraction gas stages, is necessary.

The Time-Series Interferometric Synthetic Aperture Radar (TS-InSAR), an active remote sensing technique, has got fast development in the last two decades (Berardino et al., 2003; Ferretti et al., 2011; Ferretti et al., 2001), and has been widely used in monitoring the surface displacements caused by UGS gas injection and extraction (Codegone et al., 2016; Foulger et al., 2018; Shirzaei et al., 2016; Shirzaei et al., 2019; Verdon et al., 2013). However, its application on the long-temporal ground deformation in the Hutubi gas field has rarely been reported. In this study, the large-scale background deformation near the HUGS is extracted from 16 sets of ALOS PALSAR data (2007–2010) by the small baseline subset InSAR (SBAS-InSAR) technology (Berardino et al., 2003). Then, using an improved TS-InSAR data processing strategy, we retrieve the long temporal historical displacement of the Hutubi gas reservoir from multi-track SAR datasets, including the Envisat ASAR data (2003–2010), TerraSAR-X data (2013–2015), and Sentinel-1 data (2015–2020). The obtained time-series displacement results are validated through cross-validation between the datasets and with the GNSS measurements. Thirdly, using the geological parameters of the HUGS storage, the Compound Dislocation Model (CDM) (Nikkhoo et al., 2017) is employed to quantify the spatial distribution and magnitude of the displacements caused by gas injection/extraction. Finally, the surface deformation monitoring, the deformation characteristics, the influencing factors of modeling and prediction of the gas volume and pore pressure in the Hutubi gas storage are discussed. The main findings are summarized in the Conclusions.

2. Tectonic setting and operation of the HUGS

2.1. Tectonic setting

The HUGS is located in the Changji Hui Autonomous Prefecture of Xinjiang Uygur Autonomous Region of China, about 57 km away from

Urumqi (Fig. 1). The HUGS is on the eastern part of the Manas-Hutubi fold, near the southeast-northwest strike, with the shape of an irregular cloth bag (Hu et al., 2010). It is in the second section of the Lower Tertiary Ziniquanzi formation (E_{1-2Z}) (Fig. 2). The HUGS is about 20 km long from east to west and 3.5 km wide from north to south. The central depth of the gas reservoir is about 3585 m, the original formation pressure is about 33.96 MPa, and the average formation temperature is 92.5 °C (Cao, 2013; Qiao et al., 2018). There are many blind faults, whose distribution is under debate. Pang et al. (2012) and Cao (2013) found three faults around the HUGS, named the HTB fault, HTB north fault, and Hu001 fault, as shown in Fig. 1 and Fig. 2. Jiang et al. (2020) interpreted the faults as a shear fault-bend folding, and they believed that only the HTB fault has a clear correlation with the HUGS (Fig. 1). The dip angle of the HTB fault ranges from 20° to 25°. Moreover, as shown in Fig. 2, there are five thrust-slip faults below the cretaceous (K_{2d}).

2.2. History of gas recovery and injection/extraction

The mining and evolution of the Hutubi gas field experienced five stages since the blowout in 1996: capacity-building (11/1998–11/2000), capacity stabilization (12/2000–04/2011), capacity decline (05/2011–04/2012), transformation (about 05/2011–05/2013), gas storage (06/2013 – present). The first three stages are called the gas recovery stage (Cao, 2013), and the last stage is the operation stage of the UGS after transformation.

In the gas recovery stage, the main substances extracted from the Hutubi gas field are natural gas and gas condensate, accompanied with a small amount of formation water. Seven wells worked during this stage (Fig. 1(b)). The number of working wells and formation pressure are shown in Fig. 3(a) and Fig. 3(b), respectively. During this stage, the formation pressure was reduced 20.02 MPa from 33.96 MPa, about 58.95% (Cao, 2013).

The gas reservoir transformation took nearly a year. In 06/2013, the Hutubi gas reservoir began to inject gas. The native volume of HUGS was 4.53 billion m³, but the base volume at work was 6.19 billion m³, and the design capacity was 10.7 billion m³ (Jiang et al., 2020). Currently, there are more than 30 wells related to gas injection and extraction in the HUGS (Fig. 1(b)), and 16–24 wells are working (Jiang et al., 2020). Fig. 4(a)-(b) show the photos of one well facility. By 05/2020, the HUGS has completed 7 injection and extraction cycles. Fig. 3(c) shows the average pressure change of the wellheads between 06/2013 and 04/2017 (Jiang et al., 2020). The periodic variation of wellhead pressure is highly related to gas injection/extraction, which can also reflect the internal pressure changes of the gas storage. The relationship between gas injection/extraction process and ground deformation will be discussed in Section 4.

3. Datasets and processing

To monitor and invert the complete ground deformation induced by gas recovery and gas injection/extraction in the Hutubi gas field, we collect all available InSAR datasets from multi-platform and multi-orbit over this area (Table 1). The coverage of the SAR datasets is shown in Fig. 1(a). The temporal coverage of the images is shown in Fig. 5.

3.1. The SBAS-InSAR processing

The L-band InSAR data have lower monitoring accuracy than the C- and X-band InSAR datasets, but they can restrain the spatiotemporal decoherence of the interference phase (Daniel and Lu, 2007; Hanssen, 2001). Hence, we use the L-band ALOS PALSAR images to investigate the background deformation around HUGS and the deformation characteristics of the region. First, we obtain a small baseline subset containing 27 InSAR pairs from the 16 ALOS PALSAR images, by setting an appropriate spatiotemporal baseline threshold. The small baseline net is

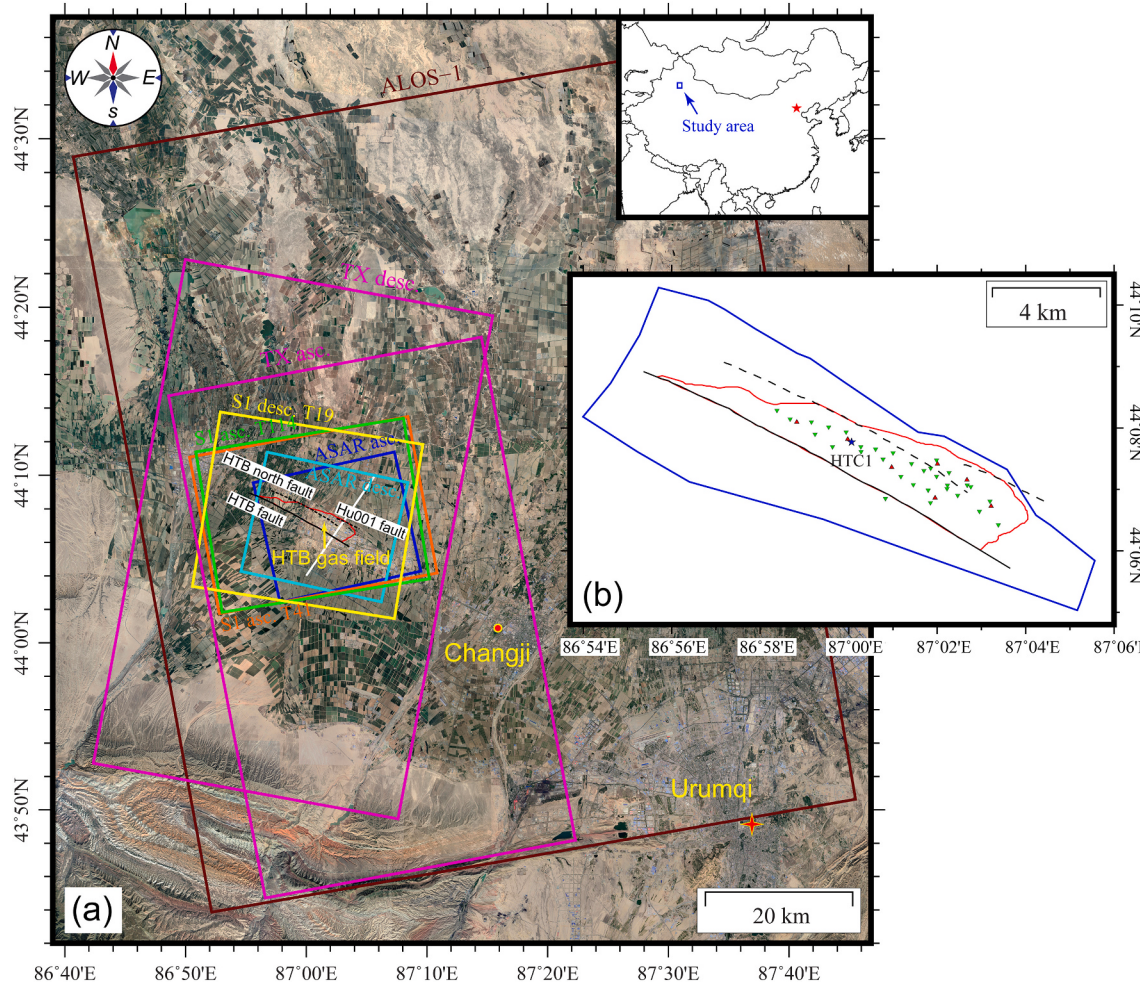


Fig. 1. The Hutubi gas field. (a) Location of the Hutubi underground gas storage and coverage of the SAR datasets. (b) Distribution of the gas recovery (red triangles), injection/extraction (green inverted triangles) wells, and the GNSS continuous station, HTC1 (blue star). Background image: Google Maps satellite image. (For interpretation of the references to colour in this figure legend, the reader is referred to the web version of this article.)

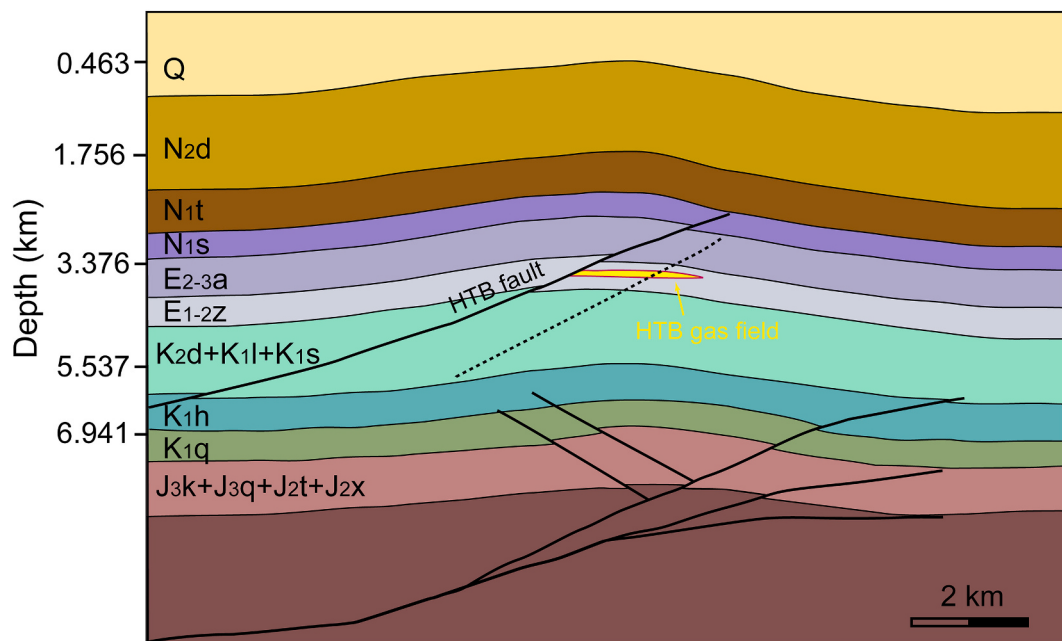


Fig. 2. The stratigraphic structure of the HUGS. The location of this profile is shown by the white solid line in Fig. 1.

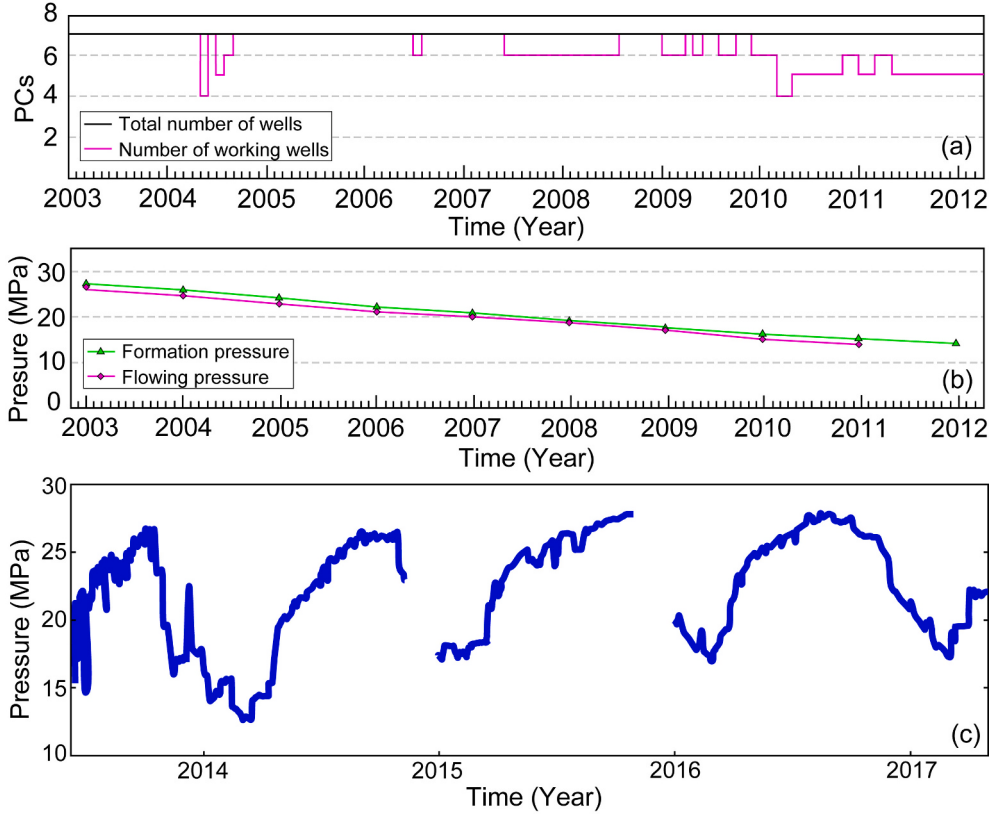


Fig. 3. (a) Number of working wells. (b) Formation pressure in the gas recovery stage. (c) The variation of the average pressure in the working wells between 06/2013 and 04/2017 (the injection/extraction stage).

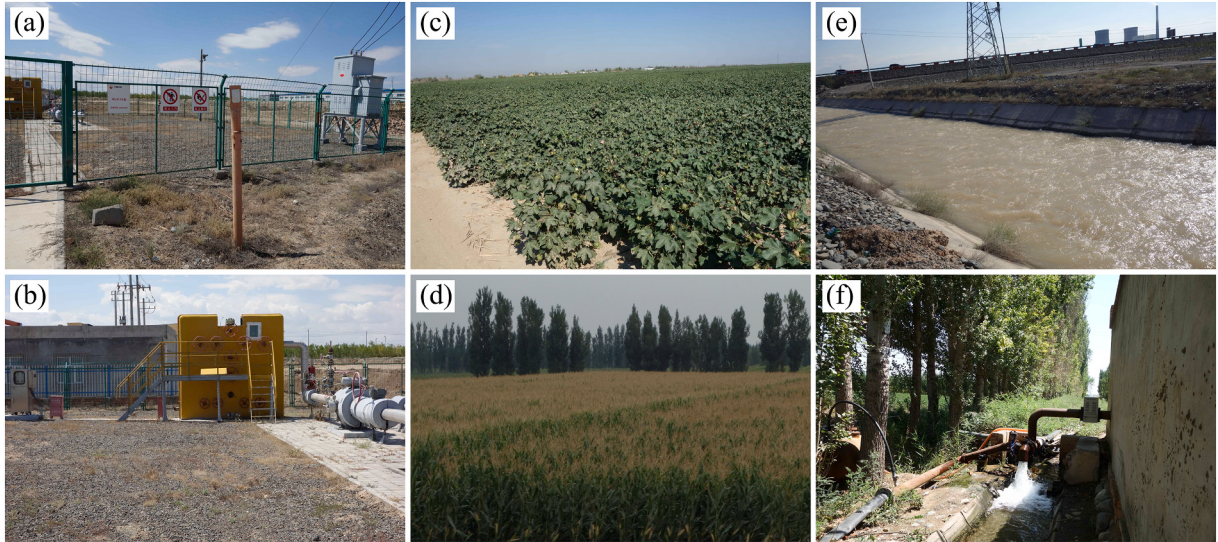


Fig. 4. Photos of (a-b) a working gas well, (c-d) crops, (e-f) a glacier-melt river and an irrigating facility in Hutubi gas field.

shown in Fig. S1. Then, the two-pass Differential InSAR (DInSAR) approach is applied to process the InSAR pairs (Zebker et al., 1994). The Shuttle Radar Topography Mission (SRTM) Digital Elevation Model (DEM) at 1-arcsec resolution (Farr et al., 2007) is employed to remove the topographic phases, and the multi-looking operation (range \times azimuth: 6 \times 16) is applied to suppress decorrelation noise. The achieved resolution in the west-east and north-south directions is about 50 m. Finally, the SBAS-InSAR technology is used to process the multiple DInSAR pairs to obtain the time-series deformation of large-scale areas.

The average displacement rate is shown in Fig. 7.

3.2. TanDEM-X processing

Using higher precision external DEM can remove the terrain phase better and achieve higher geocoding accuracy. Furthermore, the SAR images with higher resolution and shorter band wavelength are more sensitive to the terrain phase residuals and geocoding errors (Hanssen, 2001), especially the high-precision TerraSAR-X images. Hence, high

Table 1
SAR data information.

Sensors	ALOS-1	Envisat ASAR		TerraSAR-X		Sentinel-1		
Orbit	Asc.	Asc.	Desc.	Asc.	Desc.	Asc. 114	Asc. 41	Desc. 19
Time period	13/02/2007-09/ 10/2010	10/03/2007-03/ 04/2010	21/04/2003-26/ 11/2007	11/11/2013-20/ 07/2015	20/08/2013-23/ 07/2015	30/03/2015-20/ 04/2020	25/03/2015-21/ 05/2020	21/03/2015-26/ 05/2020
No. of sets	16	13	25	35	38	113	122	114
No. of int. pairs	27	25	53	105	90	344	372	334

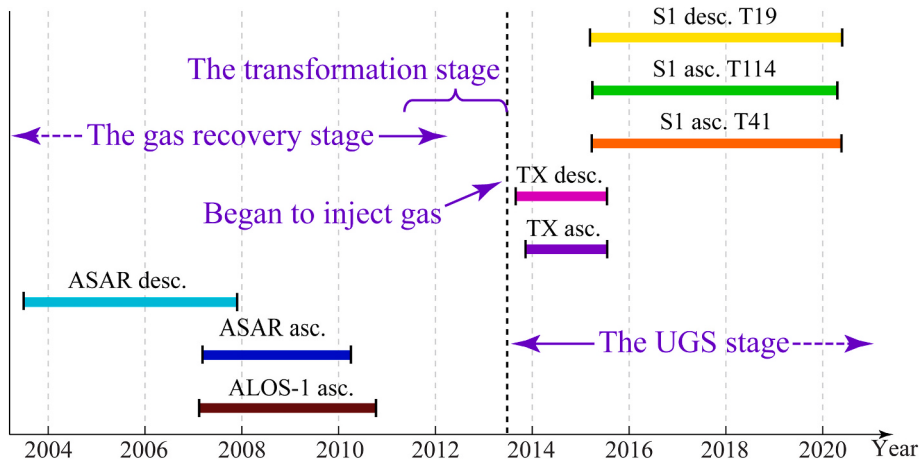


Fig. 5. Acquisition dates of the SAR images used in this study. (TX: TerraSAR-X, S1: Sentinel-1).

accuracy external DEM is very important for obtaining deformation time series. In this study, we process two TerraSAR/TanDEM-X images obtained on 13/03/2011 (Du et al., 2019) to generate a 5 m resolution DEM (Fig. 6, hereafter referred to the TanDEM). This high-precision TanDEM is used as an external DEM in the subsequent time-series displacement calculation. As shown in Fig. 6, the TanDEM has more detailed surface elevation information and stronger descriptive ability in local terrain texture than the SRTM DEM with the resolution of 1-arcsec (30 m).

3.3. IPTA-InSAR processing

We use seven C- and X-band InSAR datasets to monitor the long temporal deformation in the gas recovery and gas injection/extraction stages of the Hutubi gas field. The Envisat ASAR (C-band), TerraSAR-X

(X-band), and Sentinel-1 (C-band) datasets are processed by an improved Interferometric Point Target Analysis (IPTA) method. Considering the acquisition time and spatial resolution of the datasets, the 1-arcsec SRTM DEM is employed for the Envisat ASAR datasets (C-band) and the generated TanDEM is used for the two latter data. The multi-looking operation of 1:5, 2:2, and 5:1 in the range and azimuth directions are utilized to suppress the interferometric noise in the ASAR, TerraSAR-X, and Sentinel-1 SAR datasets, respectively. Using the available 460 SAR images, we generated 1323 interferogram pairs with the spatiotemporal baselines in the given thresholds (Table 1). The images and the spatiotemporal baseline distributions of the interferograms are given in Table S1–4 and Fig. S1. The improved IPTA technique in this study is based on the IPTA proposed by Werner et al. (2003) and GAMMA software (Werner et al., 2000). We use an optimized point selection strategy to select high-quality interferometric points (Xiong

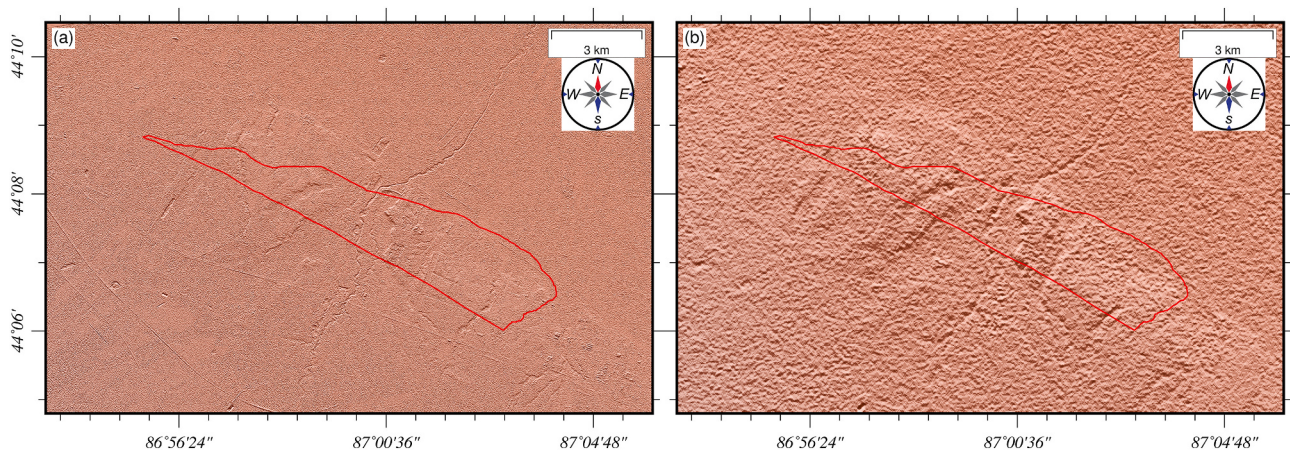


Fig. 6. The (a) 5 m and (b) 30 m resolution DEMs generated from TanDEM-X InSAR pairs and SRTM, respectively. The red line shows the location of the HUGS. (For interpretation of the references to colour in this figure legend, the reader is referred to the web version of this article.)

et al., 2020). The results of the above seven InSAR datasets are shown in Fig. 8–Fig. 10.

4. Results

4.1. Large-scale background deformation

Fig. 7 shows the average displacement rate monitored by the ALOS PALSAR dataset. Seven settling funnels (outlined by black curves) distribute north to the gas field (marked by the black curves), with the maximum subsiding rate exceeding 50 mm/yr. This region has large plantations (147,249 ha in 2018), of which 99.9% needs irrigation (Gao and Han, 2019). The main crops in this area are wheat, ensilage, alfalfa, corn, and cotton (see Fig. 4(c)–(d)). Of the water supply, 53.5% comes from surface water, 46% from groundwater extraction, and the remaining 0.5% from intermediate water (Gao and Han, 2019). Intermediate water refers to the water reclaimed from treated wastewater or rain. Fig. 4(e) and (f) show the photos of a glacier-melt river and an irrigation well in Hutubi, respectively.

The location of the subsiding funnels is highly related to the plantations, but far away from the HUGS, according to the optical satellite images and field exploration (Fig. 7). The nearest funnel to the HUGS is about 4 km away. The average deformation rate of this area is less than 3 mm/yr, so the HUGS is not affected by the settling funnels.

4.2. Long-temporal historical displacements

4.2.1. Displacements during the gas recovery stage (04/2003–04/2010)

Using the Envisat ASAR images from descending (21/04/2003–26/11/2007) and ascending orbits (10/03/2007–03/04/2010), we obtain the displacements caused by gas and oil extraction in the gas recovery stage (Fig. 8). As Fig. 8 shows, the ground surface of the whole gas field is stable, but the gas well concentrated area (in the black ellipse) has obvious subsidence. The displacement regions monitored from the two orbit datasets have similar area, but different spatial distribution and

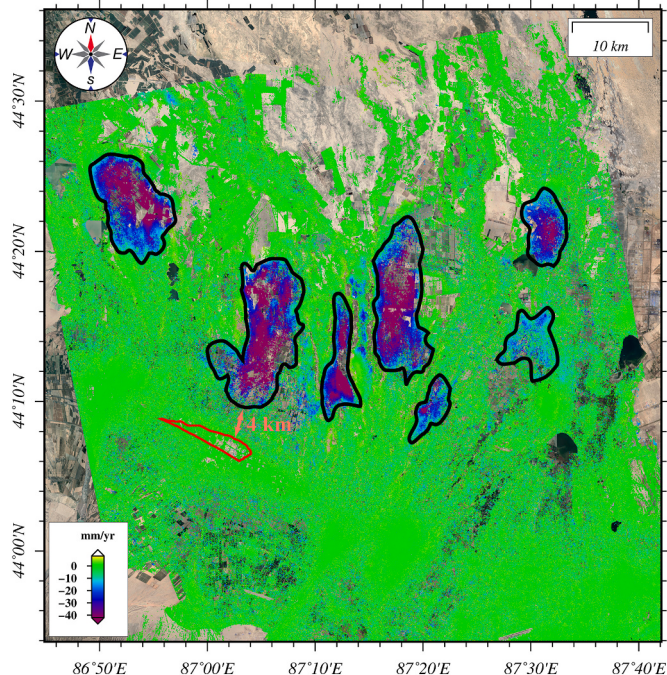


Fig. 7. The average displacement rate monitored by the ALOS PALSAR dataset. The red line outlines the position of HUGS. The black lines outline the obvious subsiding funnels in this area. (For interpretation of the references to colour in this figure legend, the reader is referred to the web version of this article.)

magnitude, due to the differences in image acquisition time and gas extraction intensity.

To quantitatively analyze the surface displacements in the gas recovery stage, we select two points (P1 and P2 in Fig. 8) to show their time-series cumulative displacements. The time-series cumulative displacements of one single point show that the results of the ascending and descending datasets have good continuity in time. The average displacements rate is about 2.2 mm/yr. In the time-series display, we unify the time datum by fitting the deformation in the time overlap range (the pale-yellow shadow in Fig. 8(c) and (d)), because those two ASAR datasets have similar incidence angles (about 22.8°).

4.2.2. Displacements during the injection/extraction stage

We extract the time-series deformation of the HUGS caused by the seasonal injection/extraction from the TerraSAR-X (08/2013–07/2015) and the Sentinel-1 (03/2015–05/2020) images (Fig. 9). Unlike the surface subsidence at the gas recovery stage (2003–2010), there is obvious ground uplift in the center of the HUGS surface. The average uplift rate in the center is about 7 mm/yr during 08/2013–07/2015 and 13 mm/yr during 03/2015–05/2020. The reason is that the gas field was converted from a gas production reservoir to a UGS in 06/2013. In the UGS early construction stage, the injected natural gas is more than the extracted (Jiang et al., 2020). This increases the reservoir internal pressure and forces the formation stress propagate to the surface, causing surface uplift.

The ground uplift center in the TerraSAR-X results is in the black ellipse in Fig. 9. The location of the deformation center observed by the Sentinel-1 datasets is close to the TerraSAR-X result, but the deformation center expands to the northwest, and the deformation area is larger, indicating that the deformation region has increased. This is mainly related to the construction and development of the gas storage. With the repetition of gas injection and extraction, the porosity of the gas reservoir medium develops and becomes stable.

4.2.3. Consistency of the TerraSAR-X and Sentinel-1 results

As Fig. 9 shows, the results of the datasets with the same acquisition time are consistent in the order of magnitude and spatial distribution, and the results generated from the datasets of different platforms (TerraSAR-X and Sentinel-1) have good consistency in spatial distribution. The cumulative deformation of three points (P1, P2, P3) was selected to explain the time-series displacements (Fig. 10). Note that the observed geometric parameters of each InSAR dataset are different, but the time span of the ascending, descending or adjacent tracks dataset of one SAR sensor is roughly the same, and the difference of the projection geometry has no effect on the inversion of model parameters in Section 5. Therefore, we use the strategy in Section 4.2.1 for time datum unification.

Superposing the well average pressure data (Fig. 3(c)) onto the time-series displacement results (Fig. 10), we found a strong temporal correlation between the well pressure change and the surface deformation. When inject gas (April to October), the well pressure rises, the formation pressure increases, and the ground uplifts fast; when extract gas (November to next March), the well pressure drops, formation pressure decreases, and the ground uplift stops or subsidence appears. The time-series results show that the surface deformation is irregular in the early gas injection/extraction stage (2013–2016). With the recycling of injection/extraction, the working pressure of the HUGS gradually becomes regular (after 2017). The ground surface deformation caused by formation pressure changes is more significant. In this stage, the injected gas is more than the extracted gas, so the surface shows continuous uplift. The cumulative displacements of P1, P2, and P3 are 62 mm, 76 mm, and 58 mm, respectively.

4.3. Accuracy assessment

To quantitatively assess the reliability and accuracy of the TS-InSAR

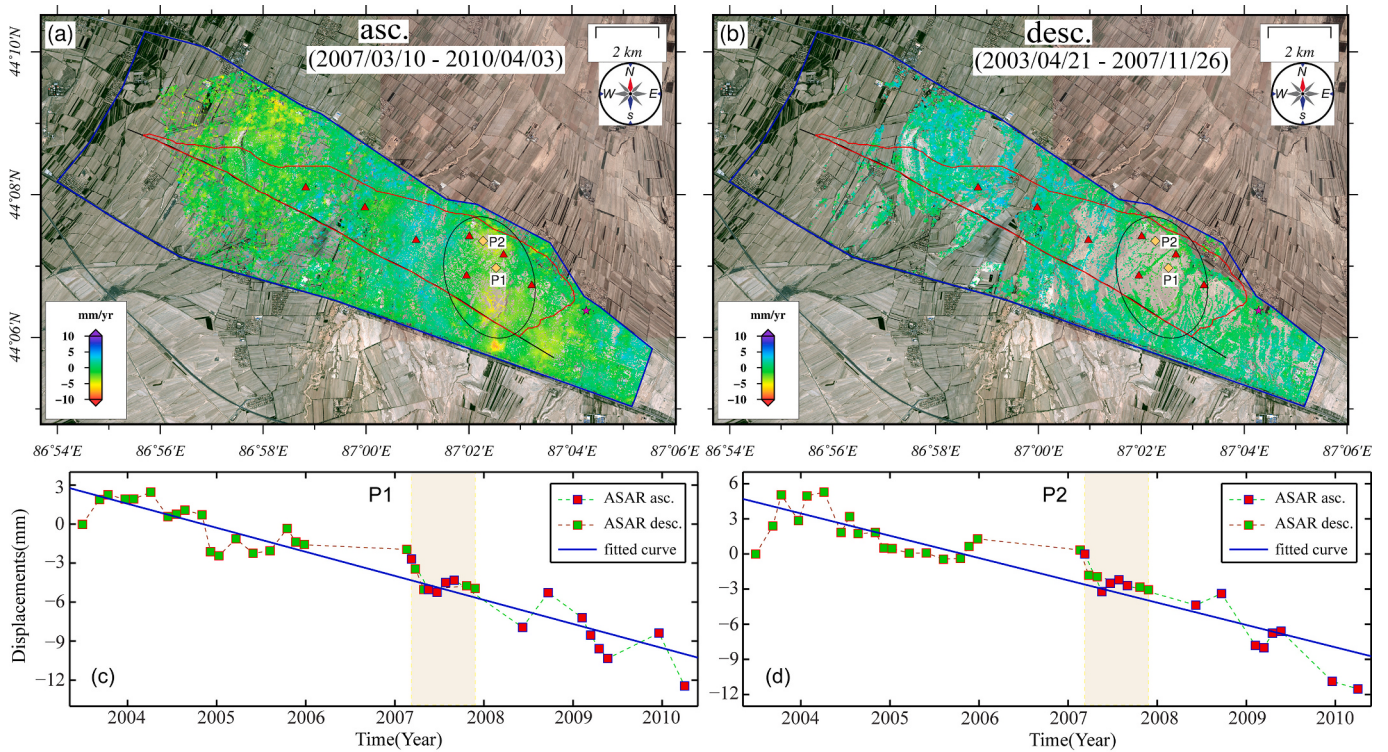


Fig. 8. The average displacement rate calculated from (a) ascending (10/03/2007–03/04/2010) and (b) descending (21/04/2003–26/11/2007) InSAR dataset. The red triangles are the gas wells and the magenta star is the unwrapping reference point. (c)(d) Time-series cumulative displacements of the two points (P1 and P2). The pale-yellow shadow shows the time-interleaving of ascending and descending track datasets. Background image: 2007 Google Maps satellite image. (For interpretation of the references to colour in this figure legend, the reader is referred to the web version of this article.)

results, we compare the average displacement rates extracted from the InSAR datasets acquired at the same period, i.e., the TerraSAR-X ascending and descending tracks datasets, and the Sentinel-1 ascending, descending, and adjacent tracks datasets. These results show good consistency (Fig. 11), with the difference at most points smaller than 3 times the root-mean-square error (RMSE) (between the red dotted lines). The correlation between TerraSAR-X ascending and descending tracks results, Sentinel-1 ascending T41 and T114, ascending T41 and descending T19, descending T19 and ascending T114 tracks results are 0.52, 0.85, 0.87, 0.84, respectively. The different observation geometry of the SAR datasets partially contributes to the result discrepancy. Nevertheless, the good consistency between the monitoring results can confirm the reliability of the TS-InSAR.

Moreover, we project the three-dimensional time-series deformation results of a GNSS continuous station (HTC1, Fig. 1(b)) to the line-of-sight (LOS) displacement of tracks T114, T41, and T19 of the Sentinel-1 datasets, and compare them with the TS-InSAR results of these three tracks (Fig. 12). The difference between the deformation rate of the HTC1 observations and the results of T114, T41, T19 tracks are 4.1 mm/yr, 2.4 mm/yr, 3.1 mm/yr, respectively. The consistency between InSAR and GNSS measurements also confirms the reliability of the time-series results.

5. Geomechanical modeling

The migration, exploitation, or injection of underground substances (such as magma, natural gas, carbon dioxide) disturb the stress balance of strata, change the stratum pore medium pressure and cause land subsidence or uplift. Those geophysical processes are usually modeled by the full/half-space theory (Okada, 1985, 1992; Shirzaei et al., 2016; Suckale, 2009; Xu et al., 2020). Nikkhoo et al. (2017) developed a generalized source model for pressurized cavities, called the compound dislocation model (CDM). This model uses three mutually orthogonal

rectangular dislocations, which are free to dip in any direction, to represent planer and volumetric source of any aspect ratios. We use the CDM to model and estimate the ground deformation caused by gas injection/extraction.

5.1. Source parameter estimation

The cumulative deformation in the LOS direction calculated from T114, T41, T19 in the same period was selected as the observation dataset. The CDM source consists of 10 parameters: centroid location (E_0, N_0, d), rotation angles ($\omega_x, \omega_y, \omega_z$), semi-axes (a, b, c), and uniform opening or closing (u). We establish the local geodetic coordinate system, taking the HUGS surface (44.1°N, 87.0°E) as the coordinate origin and the east, north, and vertical upward as the x , y , z axes, respectively. The Poisson's ratio is assumed as 0.25. The 10 parameters are unknown, so we set their original value and the value range, as shown in Table 2. The best-fitting model parameters are searched by a nonlinear simulated annealing estimation algorithm (Cervelli et al., 2001). And a randomize-then-optimize method (500 times) was applied to assess the model parameter uncertainties (Bardsley et al., 2014; Xu et al., 2020). The best-fitting parameters and the geometric model of the HUGS by the CDM model are shown in Table 2 and Fig. 13, respectively.

The estimated central depth (3499.7 m) and height (108.6 m, 2c) of the storage are consistent with the actual central depth (~3585 m) and height (~110 m). Using the best fitting CDM parameters, we found that the potency (the volume of nature gas injected into the UGS, generally larger than the volume change of the UGS) is about 1.93 million m³. The calculation formula of the potency is $Pot. = 4 \cdot (a \cdot b + a \cdot c + b \cdot c) \cdot u$. The deformation in the east-west, north-south, and up-down directions was inverted from the estimated CDM (shown in Fig. 14(g-i)) and was projected on to the imaging geometry of the three track Sentinel-1 SAR datasets, respectively (Fig. 14(d-f)). The simulated ground deformations of the three tracks have good consistency with the observed results in

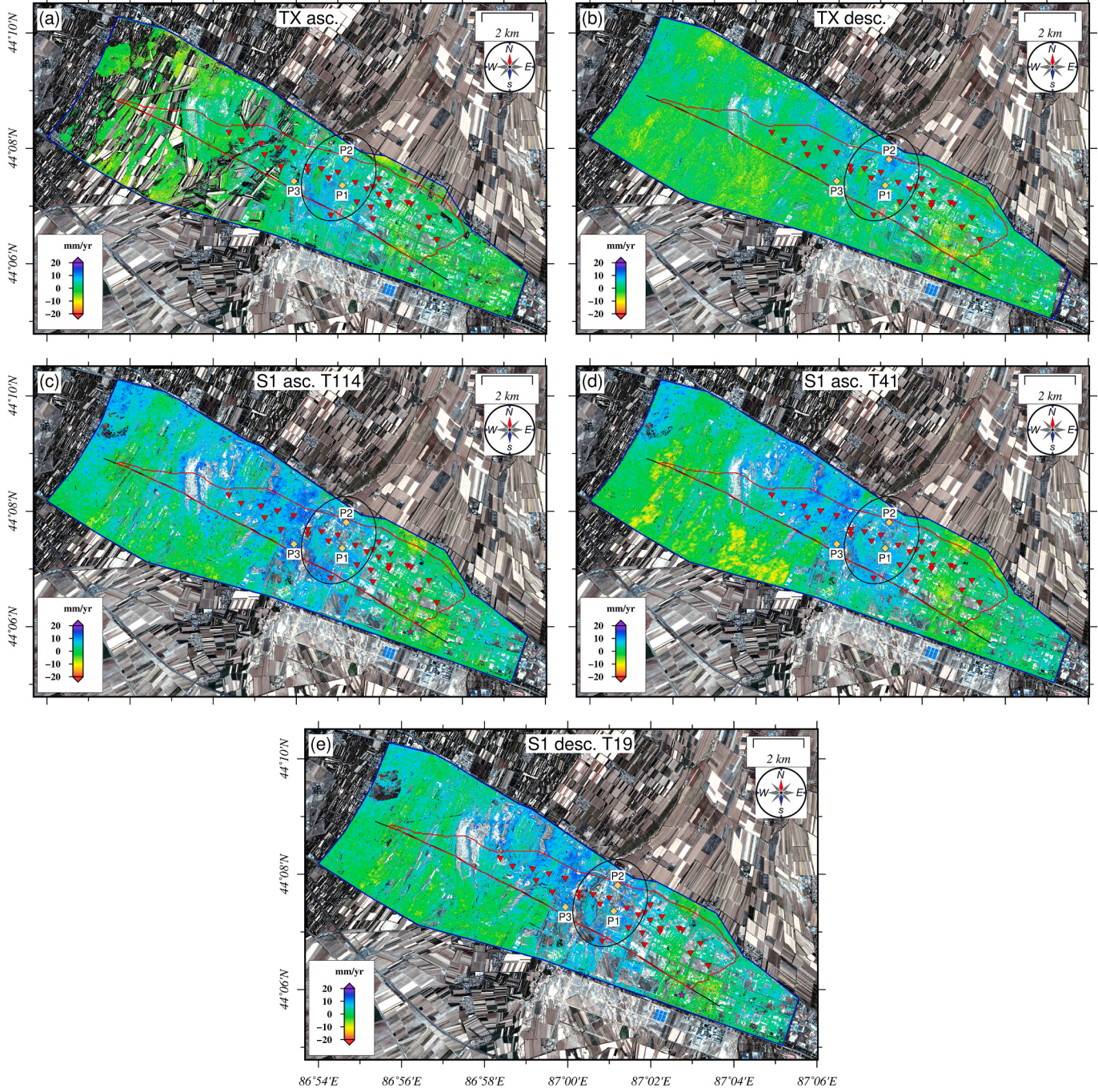


Fig. 9. The displacement rates calculated by the (a) ascending and (b) descending TerraSAR-X data, and the (c) (d) ascending (T114 and T41) and (e) descending (T19) Sentinel-1 images. The red inverted triangles indicate the gas wellheads. The yellow diamonds are the selected characteristic points. Background image: Planet satellite optical image obtained on 23/09/2016. (For interpretation of the references to colour in this figure legend, the reader is referred to the web version of this article.)

size and distribution.

5.2. Dynamic process of the gas injection/extraction

To investigate the expansion and shrinkage of HUGS caused by gas injection and extraction, we retrieve the dynamic parameter u from the time-series displacements (after 01/2017) of the Sentinel-1 T41 dataset using the known CDM geometric parameters. The dynamic opening/closing parameter, u , is estimated by the method stated in Section 5.1. The results are shown in Fig. 15, which can react to the changes in the gas reservoir volume. The simulated dynamic deformation along the

LOS direction of the Sentinel-1 T41 track geometric is presented in Gif S1.

As Fig. 15 shows, the uplift and subsidence of the ground surface are closely related to the expansion and shrinkage of the gas storage. The pressure changes caused by gas injection and extraction break the stress balance of the surrounding rock mass, resulting in the periodic uplift and subsidence of ground surface. For estimating the gas injection volume in the HUGS, we fit the opening/closing of the gas reservoir linearly (green line in Fig. 15). The gas reservoir capacity shows continuous expansion, which is consistent with the design. We calculate the opening and closing of the three complete gas injection and extraction cycles from

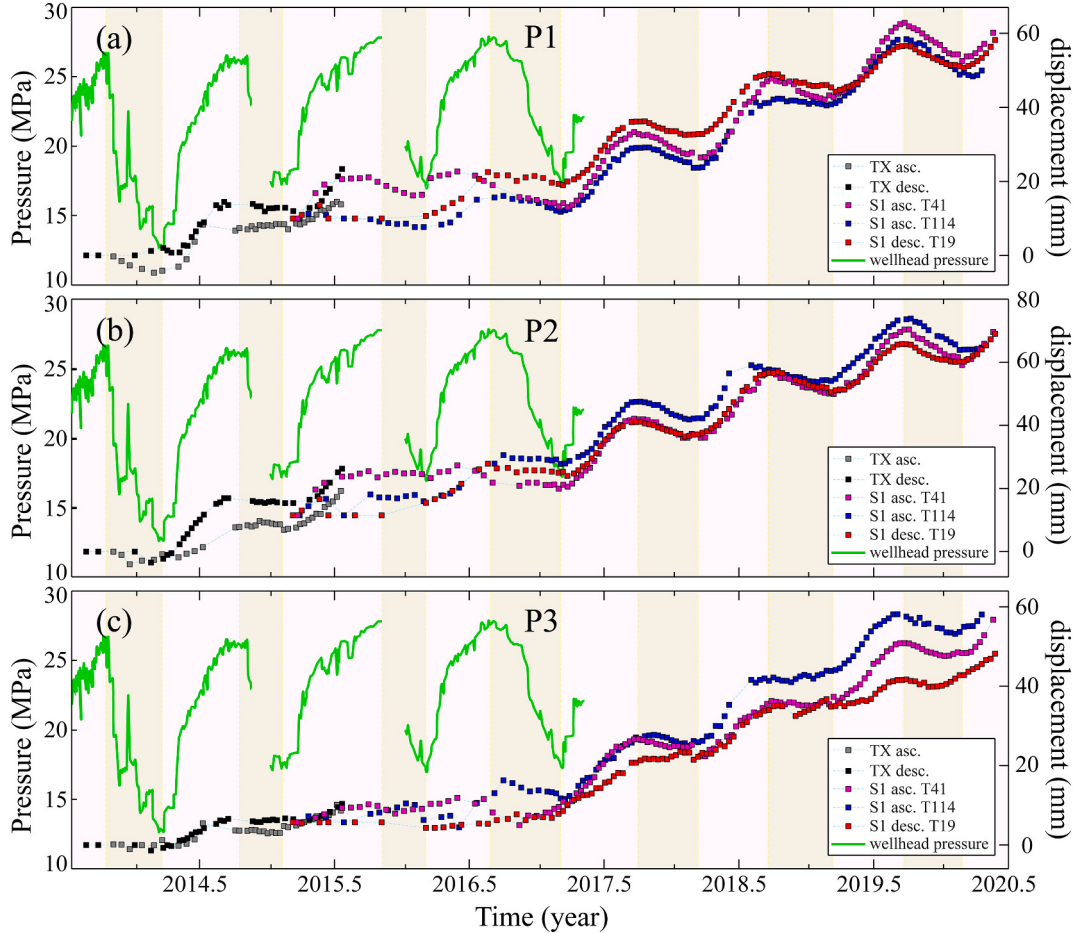


Fig. 10. The time-series cumulative displacements of three feature points (P1, P2, P3). The green lines show the average well pressure. The light-pink and light-yellow shades represent the periodic changes of the ground deformation caused by gas injection and extraction. (For interpretation of the references to colour in this figure legend, the reader is referred to the web version of this article.)

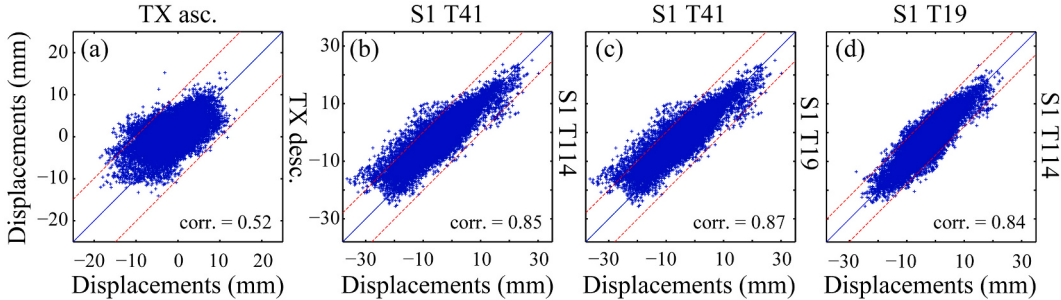


Fig. 11. Comparison between the results obtained by TerraSAR-X ascending and descending, Sentinel-1 T41 and T114, T41 and T19, T19 and T114 data. The red dotted lines denote the three times the root-mean-square error. (For interpretation of the references to colour in this figure legend, the reader is referred to the web version of this article.)

2017 to 2020 (Fig. 15). The gas storage expansion (e.g., Δu_1 , Δu_3 , Δu_5) is larger than the shrinkage (e.g., Δu_2 , Δu_4 , Δu_6) in each cycle. However, the shrinkage is gradually increasing ($\Delta u_2 < \Delta u_4 < \Delta u_6$) and the expansion becomes stable ($\Delta u_{\text{inject.}} \approx 0.162$), indicating that the gas storage is about to reach the equilibrium state of injection and extraction. With the operation of the HUGS, when the designed volume is reached (e.g., the base volume and the design capacity), the gas injection and extraction volume will be balance.

5.3. Coupling between surface displacements and gas reservoir volume change

To highlight the coupling relationship between the gas injection/extraction process and the ground surface displacements, we separate the corresponding nonlinear component from the dynamic changes of P2 and u in Fig. 15. Specifically, we firstly fit the linear component (e.g., the green line in Fig. 15), and then remove them. The remain is the nonlinear components of their changes (Fig. 16). Moreover, we collected the gas injection schedules of HUGS during 2017–2020 (Table S5) and superimposed them on Fig. 16. As Fig. 16 shows, the reservoir expansion

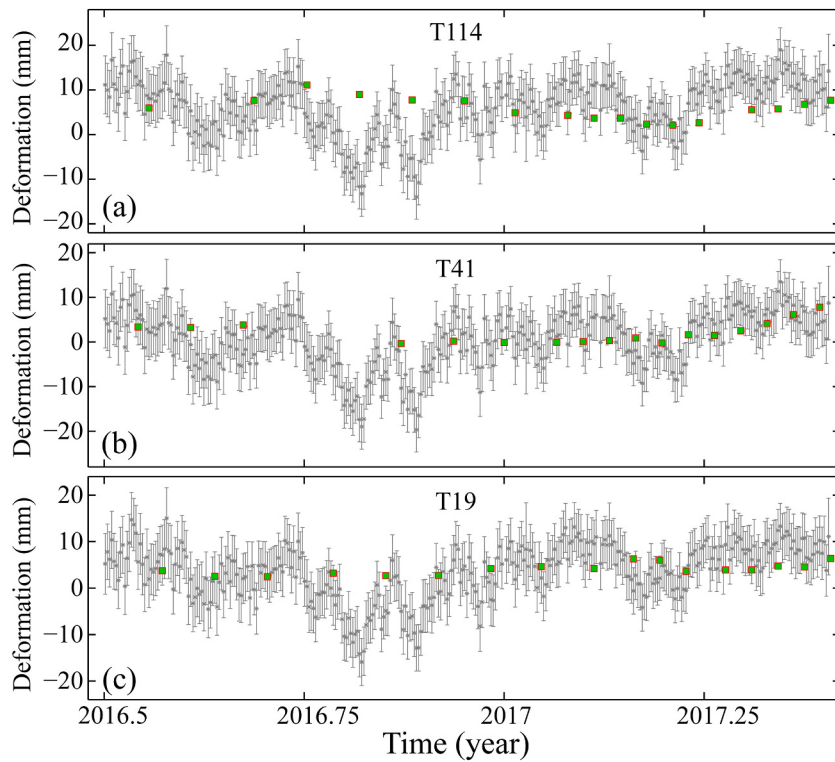


Fig. 12. Comparison between the time-series InSAR results (green squares) and the GNSS observation (grey asterisk). (For interpretation of the references to colour in this figure legend, the reader is referred to the web version of this article.)

Table 2
The inverted CDM model parameters.

Parameter	E_0	N_0	d	ω_x	ω_y	ω_z	a	b	c	u
Unit	m	m	m	°	°	°	m	m	m	m
Original	0	0	3500	0	0	-44	740	2000	55	-0.2
Range	[-1000,1000]	[-1000, 1000]	[800, 4000]	[-20,20]	[-20, 20]	[-70, -20]	[50, 900]	[500, 2500]	[20, 90]	[-1, -0.001]
Best fit.	-4.5 ±2.5	-0.7 ±2.6	3499.7 ±2.4	6.4 ±0.4	-11.6 ±0.5	-48.1 ±0.8	741.1 ±2.2	2049.9 ±2.5	54.3 ±1.6	0.289 ±0.002

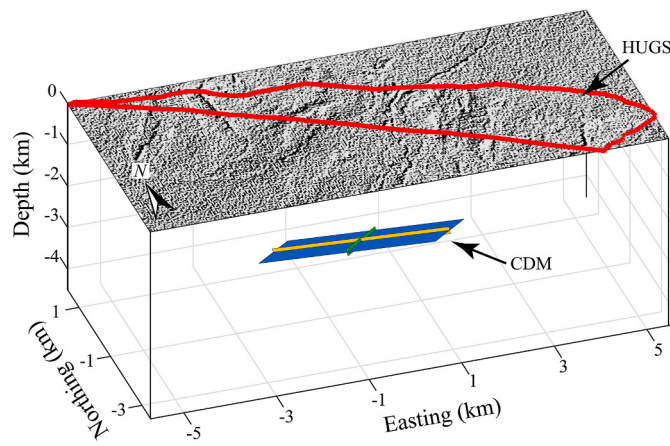


Fig. 13. The inverted CDM model geometry.

and surface uplift are coincident with the gas injection schedule. In addition, the gas extraction and balance stages correspond to the reservoir shrinkage and surface subsidence. The subsidence accelerates significantly during the extraction stage. The balance stage also has reservoir shrinkage, because the internal gas continuously spreads in the

formation pores after gas injection/extraction. The internal pressure of the gas reservoir tends to balance, which reduces the net pressure of the gas reservoir on the upper overburden.

We also collected the local monthly mean temperature of Hutubi County from 2017 to 2020 (Fig. 16(b)) and found that the temperature has a strong correlation with the gas reservoir operation. When the temperature is above ~ 10 °C, the gas is injected into the HUGS. When the temperature is below ~ 0 °C, the gas is extracted to maintain a stable gas supply (the red dotted lines in Fig. 16). The lowest temperature corresponds to the largest gas extraction rate in each cycle (the black dotted lines in Fig. 16). Therefore, the ground temperature can be taken as a reference for gas injection/extraction, which corresponds to the function of UGS.

6. Discussion

6.1. Surface displacement monitoring of gas storage

Qiao et al. (2018) processed the TerraSAR-X dataset spanning from 29/08/2013 to 13/03/2015 to monitor the deformation of the HUGS (in an area smaller than 20 km^2) with a 90 m-resolution external DEM. The external DEM may have impacts on differential interferometry and time-series deformation calculation, such as the fine registration of geocoding, terrain residual rejection, and time compliance due to surface changes. To demonstrate the effects of different resolution external

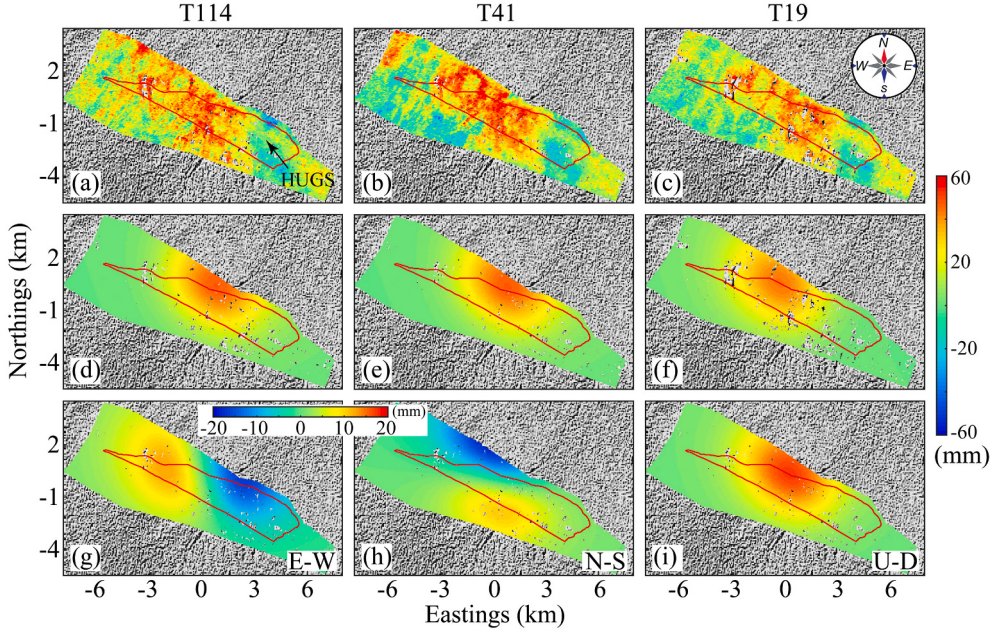


Fig. 14. (a-c) the cumulative ground deformation in the LOS direction calculated from track T114, T41, and T19 of Sentinel-1 datasets, respectively. (d-f) the simulated ground cumulative deformation in the LOS direction of the three tracks, respectively. (g-i) the simulated three-dimensional deformation of the HUGS in the east-west, north-south, and up-down directions, respectively.

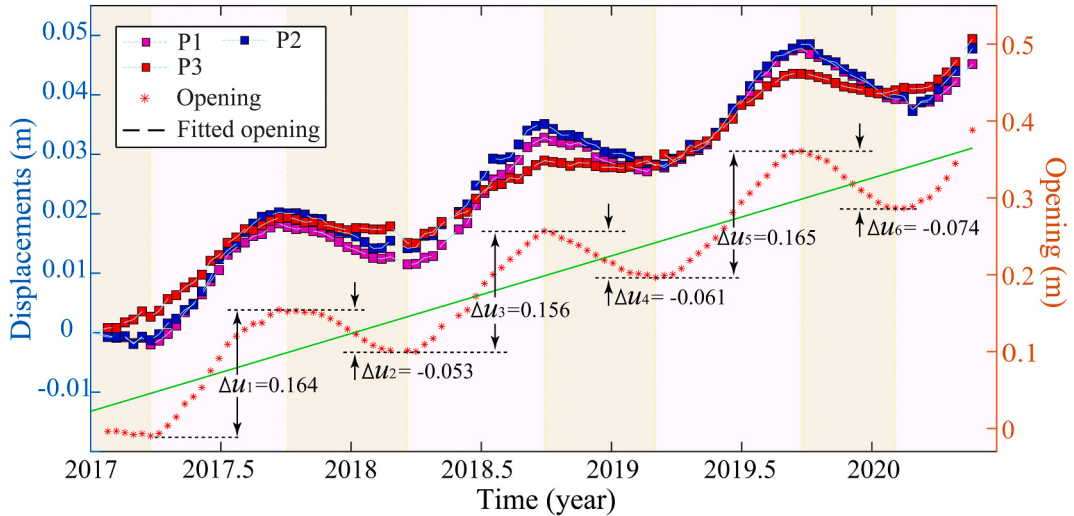


Fig. 15. Dynamic change of the opening (u). P1, P2, P3 are the temporal cumulative deformation of the three feature points obtained by the Sentinel-1 T41 dataset. The green line is the trend fitting results of u . (For interpretation of the references to colour in this figure legend, the reader is referred to the web version of this article.)

DEMs on differential interferometry, we generated one interferogram of TerraSAR-X images with the SRTM DEM and one with the generated TanDEM (Fig. 17). In the area with great topographic relief (the black ellipses), the results generated with the SRTM DEM contain more errors related to the terrain. Therefore, TanDEM, which has a higher resolution than the SRTM DEM, can bring higher geocoding accuracy and more accurately describe the local topography of the area of interest (AOI) (Du et al., 2017a; Du et al., 2017b). Besides, the acquisition time of the TanDEM (13/03/2011) is much closer to that of SAR data than the SRTM data (02/2000). Therefore, using the external DEM with better timeliness and higher accuracy brings more accurate results, especially when high-precision SAR images (e.g., TerraSAR-X) are used for a small research area (such as the Hutubi gas field) monitoring.

Many technologies have been used to monitor the deformation in the

HUGS. Leveling and GNSS can get accurate deformation around the monitoring stations, but the spatio-temporal resolution of the monitoring results is low (Qiao et al., 2018). InSAR can obtain large-scale background deformation near the AOI, and can also accurately map the local time-series deformation of the AOI. Due to these unique advantages, InSAR has become an important tool for gas storage monitoring. In this study, we used multitrack and multisensor SAR datasets and generated the large-scale background deformation and the displacement time series of the HUGS in 2003–2020 by an advanced TS-InSAR data processing strategy. Our study indicates that TS-InSAR can be used in UGS deformation monitoring, and can obtain more deformation information than the traditional in-situ measurement methods.

The TS-InSAR technology can obtain the whole-domain time-series deformation in the AOI, but it is insensitive to the horizontal movement

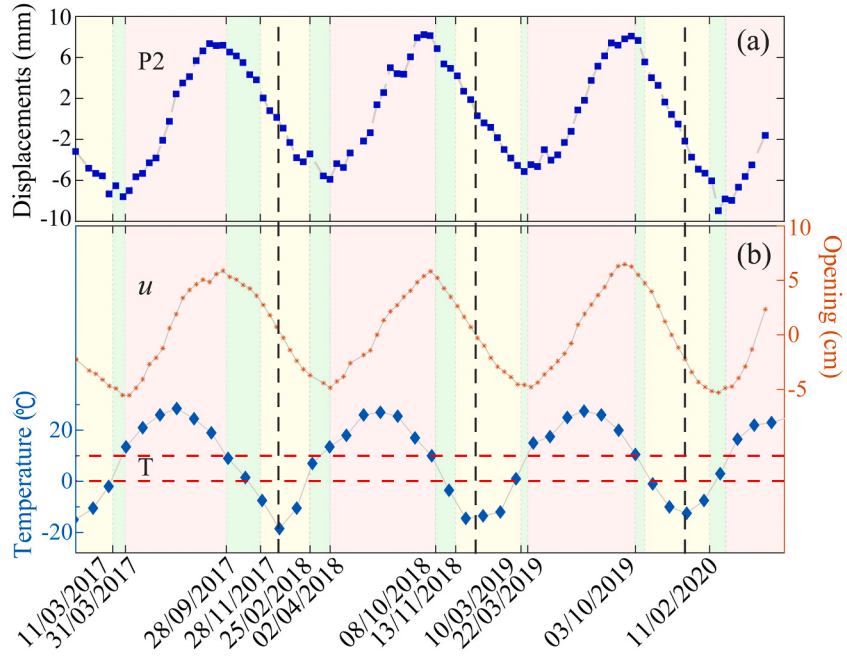


Fig. 16. The relationship between the nonlinear variation of the displacements (a) and the opening, and the temperature (b). Light-red, light-green, and light-yellow shadows indicate the gas injection stage, balance stage, and extraction stage, respectively. (For interpretation of the references to colour in this figure legend, the reader is referred to the web version of this article.)

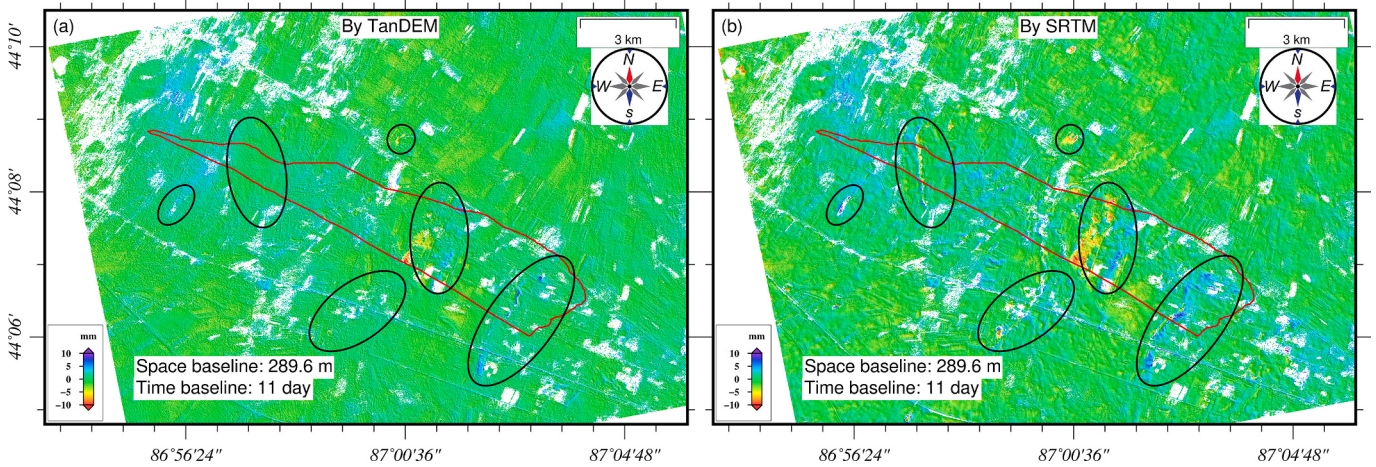


Fig. 17. The DInSAR results estimated using (a) the TanDEM and (b) the SRTM DEM.

and only gets the one-dimensional LOS deformation from the three dimension surface displacement projection, which is not sufficient to describe the deformation characteristics in the gas reservoir area. Therefore, using only InSAR technology cannot accurately describe the ground deformation in the gas reservoir area with large horizontal deformation. Even both the ascending and descending datasets are used, the insensitivity to the north-south deformation component introduces great uncertainty in the observation (Hu et al., 2014). Therefore, we use the InSAR technology to investigate the large-scale background deformation, by which the key monitoring area can be determined to guide the layout of ground survey stations and routes. Then, we can accurately monitor and describe the ground deformation by combining InSAR and ground in-situ measurements (such as leveling and GNSS).

6.2. Deformation characteristics during gas injection/extraction

The obtained long-term sequence surface deformation of the Hutubi

gas field shows that the oil and gas exploitation lasting for 14 years has caused small magnitude subsidence. The average displacement rate is about only 2.2 mm/yr, because of the large depth of the reservoir (about 3585 m in the center) and the slow formation pressure drop. As stated in Section 2.2, during the ASAR monitoring period, the Hutubi gas field was in a stable production stage, with the peak production from November to next March, and the low production from May to August (Cao, 2013). The periodic variation of the extraction intensity has been manifested in the time-series results, as the subsidence accelerates in winter and spring, and slight uplift appears in summer and autumn (Fig. 8).

In 06/2013, the gas field was transformed into a UGS, and started gas injection. After 14 years' gas extraction, the internal pressure of the gas storage is low (13.2 MPa). To improve the effectivity of gas storage and the seasonal peak-shaving efficiency, it is necessary to stabilize and increase the internal pressure to a reasonable range (18–34 MPa) (Jiang et al., 2020). The TerraSAR monitoring results (Fig. 9(a)(b)) and the

single point time-series cumulative deformation (Fig. 10) show that the surface of the HUGS kept uplifting slowly in 2013–2016. This is because the caprock lithology (such as porosity, permeability, tensile/compressive strength) is in a good condition at the early stage of the HUGS, which is unlike to cause stress accumulation and volume change. In the HUGS, the residual oil and gas, water vapor, and injected gas reached a mixed dynamic equilibrium (Chen et al., 2016). These factors combined with the great depth of the HUGS lead to a weak ground surface reaction. As Fig. 1(b) shows, the gas injection wells are evenly distributed above the HUGS, but only a few wells worked in the early stage. With the advance of injection/extraction and the stabilization of the storage internal environment, the working gas volume increased, and the number of working wells increased to 24 in 2015 (Jiang et al., 2020). The crustal stress change caused by periodic gas injection/extraction became more significant on the ground surface.

Codegone et al. (2016) studied a UGS in a depleted gas field in the Po Plain (Italy). With a depth of 1200 m, the UGS has been in operation for about 30 years. They found that in recent years the surface shows periodic uplift and subsidence corresponding to the periodic gas injection and extraction, and there is no obvious time gap between gas injection/extraction and ground deformation. Furthermore, the uplift and subsidence tend to be equal, and the ground is relatively stable (Codegone et al., 2016). The HUGS began operation in 2013, so it is still in the initial stage of construction now. We infer that after several extraction/injection cycles, the HUGS will achieve a state similar to the Po Plain UGS, that is, the surface has periodic uplift and subsidence, but the uplift and subsidence tend to be equal.

6.3. Modeling of the gas injection/extraction process

The internal spatial structure and gas storage medium of the UGSs in depleted oil and gas reservoirs are extremely complex. Gas is usually stored in the rock pores rather than in a tank-like homogeneous cavity. The gas storage capacity and exchange efficiency of a reservoir are related to porosity, permeability, roar channel (pore throat in rock), and water sensitivity of the reservoir rock (Cao, 2013). The lithology of the HUGS is dominated by siltstone and argillaceous siltstone. As the gas storage layer is heterogeneous, it is difficult to model the real gas injection/extraction process. Besides, the HUGS depth is very large, the heterogeneity can be neglected. Therefore, we take the HUGS as a homogeneous cavity to estimate the CDM parameters. Our model has achieved good application in gas storage and the 3-D deformation simulation, and can reflect the gas injection and extraction process.

Jiang et al. (2020) proposed a 2-D geomechanical model for the HUGS. They simulated and analyzed the dynamic gas injection/extraction, the surface deformation, and Coulomb stress perturbation in a vertical section of the HUGS (the white solid line in Fig. 1(a)). In their results, the radius of the affected area is 3 km, which is consistent with our results (Fig. 14). The HUGS is in an industrial area that has small groundwater demand, but there may be pockets of groundwater extraction and local subsidence. Our InSAR monitoring results show a small region with land subsidence in the eastern part of the HUGS, close to the GNSS stations used in Jiang et al. (2020). Jiang et al. considered this subsidence in their model. However, their model cannot well describe the spatial distribution of the deformation, due to the low spatial resolution of the input data (i.e., sporadic observations at several points or single profile). Nevertheless, both the CDM model and Jiang's model can reflect the dynamic gas injection/extraction of the HUGS, and the modeling results are consistent in the influence area radius and deformation periodicity.

Near the HUGS, the surface deformation is mainly caused by gas injection and extraction, but complex geological and human activities, especially excessive exploitation of shallow groundwater also contribute to the local surface deformation. According to Qiao et al. (2018) and Jiang et al. (2020), the ground subsidence caused by groundwater exploitation accelerates in summer, and slows down or even turns to

uplift in winter. Such variation is contrary to that of the periodic deformation caused by gas injection and extraction. Therefore, the contribution of large-scale groundwater exploitation to land subsidence also should be considered. It may reduce or cancel the seasonal deformation caused by gas injection and extraction, which may lead to underestimation, misunderstanding and even wrong conclusion of ground deformation.

6.4. Prediction of the gas volume and pore pressure

The gas volume and pore pressure are important parameters for UGS safety operation. Jiang et al. (2021) obtained the gas volume and corresponding pore pressure changes of the HUGS during the first 5.5 gas injection/extraction cycles (Fig. 18(a)). The gas volume and pore pressure change datasets from 31/03/2017 to 08/10/2018 (light-green span in Fig. 18(a), coincides with the dynamic change of the opening in Fig. 15) were used to fit those relationships. We uniformly select 13 volume and pressure points in the dataset (green and magenta dots in Fig. 18(a)), and find a significant linear correlation between them (blue dots in Fig. 18(b)). As stated in Section 5.1, the potency value inverted by CDM (referred to the CDM potency) is also related to the gas injection volume. To explore the relationship of the potency, the pore pressure and gas volume, the CDM potency at the acquisition time of these 13 points was correlated to the pore pressure and gas volume changes. The result shows a strong correlation between them. Thus, the linear models between the pore pressure, gas injection volume, and CDM potency are obtained (the red lines in Fig. 18(c-d)).

On the basis of these obtained linear models (Fig. 18), the dynamic changes of the pore pressure and the injected gas volume during the 5–7 cycles (Fig. 19) can be retrieved. In 12/2017, the gas inventory in HUGS was $95.77 \times 10^8 \text{ m}^3$ (Liu et al., 2019), and the corresponding forecast value is $91.29 \times 10^8 \text{ m}^3$, with a deviation of about 4.7%, indicating good agreement between the predicted and monitored values. From the predictions, the gas injection volume and the working pressure of HUGS are now close to the designed maximum value, which is consistent with the practice (Jiang et al., 2021; Liu et al., 2019). The predicted maximum gas injection volume and pore pressure at the end of the seventh injection cycle (around early 10/2019) reached 11.2 billion m^3 and 36 MPa, respectively, which are 4.8% and 5.9% larger than the design threshold, respectively.

The capacity and pressure of the HUGS predicted by the CDM and the estimated linear model may have bias, because of the rough input data and the simple linear model. The actual relationship between the CDM potency model and the gas injection volume (or the pore pressure) is very complicated (Teatini et al., 2011). Furthermore, many factors, such as the accuracy of the InSAR measurement, the geometry of the CDM model, and the structure of the crustal, also affect the prediction accuracy. Hence, a more accurate quantitative analysis needs more precise observation and an accurate model. Here only utilizing the InSAR measurements to predict the first-order function of gas volume and pore pressure provides a useful reference for the safe operation of the HUGS and other similar gas reservoirs.

7. Conclusions

We investigated the large-scale background deformation and retrieved the temporal and spatial evolution of the long temporal deformation in the Hutubi gas field. The results demonstrate that the HUGS is not affected by the large-scale settling funnels, and the deformation in this area has a significant correlation with the exploitation history. The deformation developed in two stages. In stage one, the ground subsidence was caused by oil and natural gas exploitation. In stage two, the gas field was transformed into a UGS, and the surface showed periodic uplift and subsidence related to gas injection and extraction. The monitoring results show that the subsidence in the Hutubi gas field is slow and small. At the initial operation stage of the

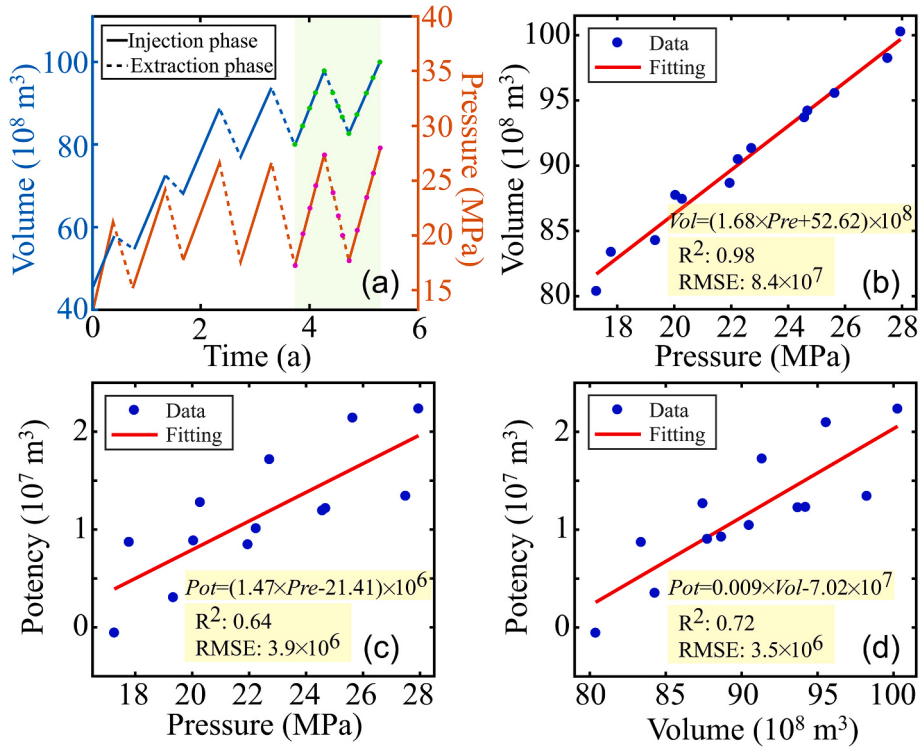


Fig. 18. Relationship between the formation pressure, gas injection volume, and gas storage potency.

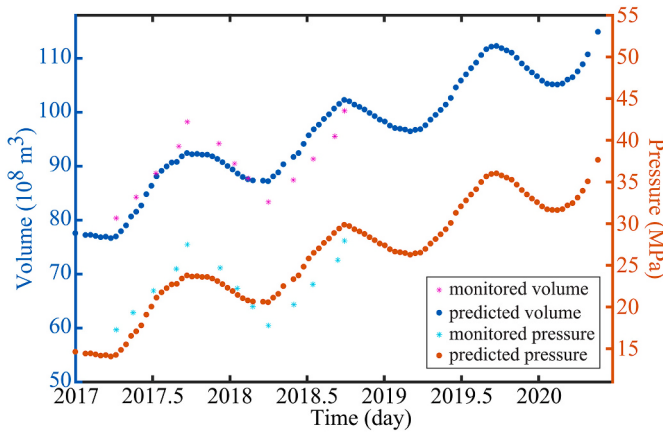


Fig. 19. The predicted formation pressure and gas injection volume.

UGS (2013–2016), the surface deformation is not obvious, because oil, gas, and water are in a mixed dynamic equilibrium state. However, with the increase and regularization of gas injection and extraction, the surface deformation becomes significant (especially after 2017). The cross-validation between independent observations of each orbit shows that the correlation between TerraSAR-X ascending and descending, Sentinel-1 ascending T41 and T114, ascending T41 and descending T19, descending T19 and ascending T114 tracks results are 0.52, 0.85, 0.87, 0.84, respectively. Moreover, the InSAR and GNSS results show the same trend of ground surface deformation. The difference between the deformation rate of GNSS observations and the results of T114, T41, T19 tracks are 4.1 mm/yr, 2.4 mm/yr, 3.1 mm/yr, respectively.

The CDM was used to model the ground deformation associated with the HUGS gas injection and extraction. The geometric parameters of the CDM model were inverted from three tracks of Sentinel-1 datasets. We obtained the dynamic expansion and shrinkage of the HUGS and the corresponding ground dynamic uplift and subsidence. The inverted

parameters and the known geological parameters of the HUGS have good consistency in depth, range, and dynamic process of gas injection and extraction. Moreover, by calculating and fitting the parameter of opening/closing (u), we found that the HUGS is now in the expansion stage, but the shrinkage is increasing gradually and the expansion becomes stable. This indicates that the gas injection and extraction are going to reach the equilibrium state. We infer that the HUGS will reach a dynamic equilibrium between opening and closing after a few years, i.e., the overall average deformation rate of the surface will tend to be zero. Finally, the gas injection volume and the pore pressure change dynamics were predicted. The predicted gas volume of the HUGS in 12/2017 is $91.29 \times 10^8 \text{ m}^3$, which is 4.7% smaller than the real gas inventory of $95.77 \times 10^8 \text{ m}^3$. The predicted maximum gas injection volume and pore pressure at the end of the seventh injection cycle are 11.2 billion m^3 and 36 MPa, respectively.

This study provides a prototype scheme for retrieving and modeling the whole-domain and long-temporal ground deformation induced by nature gas injection and extraction in UGS. Using multiple InSAR data, we can get a clear understanding of the long-term deformation history and development trend of the UGS. Moreover, considering the stratigraphic structure, temperature, precipitation, shallow/deep ground-water exploitation, and local anthropogenic disturbances will improve the monitoring and modeling of the deformation associated with UGS operations, which is also the focus of our future researches.

Declaration of Competing Interest

The authors declare that they have no known competing financial interests or personal relationships that could have appeared to influence the work reported in this paper.

Acknowledgments

We thank the Editor, the Associate Editor, and the three anonymous reviewers for their constructive comments that help us to improve the manuscript. This work was supported by the National Key R&D Program

of China (No. 2018YFC1503603) and the National Natural Science Foundation of China (Nos. 41574005), the Scientific Research Innovation Project for Graduate Students in Hunan Province (CX20200111), and the Fundamental Research Funds for the Central Universities of Central South University (2020zzts168). The authors would like to thank European Space Agency (ESA) for providing free and open ASAR and Sentinel-1 data, the Japan Aerospace Exploration Agency (JAXA) for providing the PALSAR images (No: PER2A2N038), and the German Space Agency (DLR) for kindly providing the TerraSAR-X images (No: MTH2107).

Appendix A. Supplementary data

Supplementary data to this article can be found online at <https://doi.org/10.1016/j.rse.2021.112768>.

References

- Bardsley, J.M., Solonen, A., Haario, H., Laine, M., 2014. Randomize-then-optimize: a method for sampling from posterior distributions in nonlinear inverse problems. *SIAM J. Sci. Comput.* 36, A1895–A1910.
- Berardino, P., Fornaro, G., Lanari, R., Sansosti, E., 2003. A new algorithm for surface deformation monitoring based on small baseline differential SAR interferograms. *IEEE Trans. Geosci. Remote Sens.* 40, 2375–2383.
- Cao, X., 2013. A Research on Reservoir Geomechanics Features of a Gas Storage in Xinjiang after Natural Depletion. China University of Geoscience, Beijing.
- Cervelli, P., Murray, M.H., Segall, P., Aoki, Y., Kato, T., 2001. Estimating source parameters from deformation data, with an application to the March 1997 earthquake swarm off the Izu Peninsula, Japan. *J. Geophys. Res. Solid Earth* 106, 11217–11237.
- Chen, W., Yu, P., Xiong, W., Li, J., Feng, G., Qiao, X., 2016. InSAR deformation monitoring and simulation of underground gas storage in Hutubi, Xinjiang. *J. Geodes. Geodyn.* 36, 803–812.
- Codegone, G., Rocca, V., Verga, F., Coti, C., 2016. Subsidence modeling validation through back analysis for an Italian gas storage field. *Geotech. Geol. Eng.* 34, 1749–1763.
- Daniel, D., Lu, Z., 2007. Interferometric Synthetic-Aperture Radar (InSAR). Springer, Berlin, Heidelberg.
- Ding, G., Wei, H., 2020. Review on 20 years' UGS construction in China and the prospect. *Oil & Gas Storage Transp.* 39 (373), 32–38.
- Du, Y., Feng, G., Li, Z., Peng, X., Zhu, J., Ren, Z., 2017a. Effects of external digital elevation model inaccuracy on StaMPS-PS processing: a case study in Shenzhen, China. *Remote Sens.* 9, 1115.
- Du, Y., Zhang, L., Feng, G., Lu, Z., Sun, Q., 2017b. On the accuracy of topographic residuals retrieved by MTInSAR. *IEEE Trans. Geosci. Remote Sens.* 55, 1053–1065.
- Du, Y., Feng, G., Li, Z., Peng, X., Ren, Z., Zhu, J., 2019. A method for surface water body detection and DEM generation with multigeometry TanDEM-X data. *IEEE J. Select. Top. Appl. Earth Observ. Remote Sens.* 12, 151–161.
- Farr, T.G., Rosen, P.A., Caro, E., Crippen, R., Duren, R., Hensley, S., Kobrick, M., Paller, M., Rodriguez, E., Roth, L., Seal, D., Shaffer, S., Shimada, J., Umland, J., Werner, M., Oskin, M., Burbank, D., Alsdorf, D., 2007. The shuttle radar topography mission. *Rev. Geophys.* 45, RG2004.
- FERRETTI, A., PRATI, C., ROCCA, F., 2001. Permanent Scatterers in SAR interferometry. *IEEE Trans. Geosci. Remote Sens.* 39, 8–20.
- FERRETTI, A., FUMAGALLI, A., NOVALI, F., PRATI, C., ROCCA, F., RUCCI, A., 2011. A new algorithm for processing interferometric data-stacks: SqueezSAR. *IEEE Trans. Geosci. Remote Sens.* 49, 3460–3470.
- Foulger, G.R., Wilson, M.P., Gluyas, J.G., Julian, B.R., Davies, R.J., 2018. Global review of human-induced earthquakes. *Earth Sci. Rev.* 178, 438–514.
- Gao, W., Han, R., 2019. Xinjiang Statistical Yearbook-2019. China Statistics Press.
- Hanssen, R.F., 2001. Radar Interferometry: Data Interpretation and Error Analysis. Springer, Berlin.
- Hu, G., Zhang, S., Li, J., Li, J., Han, Z., 2010. The origin of natural gas in the Hutubi gas field, Southern Junggar Foreland Sub-basin, NW China. *Int. J. Coal Geol.* 84, 301–310.
- Hu, J., Li, Z.W., Ding, X.L., Zhu, J.J., Zhang, L., Sun, Q., 2014. Resolving three-dimensional surface displacements from InSAR measurements: a review. *Earth Sci. Rev.* 133, 1–17.
- Hu, B., Li, H., Zhang, X., Fang, L., 2020. Oil and gas mining deformation monitoring and assessments of disaster: using interferometric synthetic aperture radar technology. *IEEE Geosci. Remote Sens. Mag.* 8, 108–134.
- Jiang, G., Qiao, X., Wang, X., Lu, R., Liu, L., Yang, H., Su, Y., Song, L., Wang, B., Wong, T.-f., 2020. GPS observed horizontal ground extension at the Hutubi (China) underground gas storage facility and its application to geomechanical modeling for induced seismicity. *Earth Planet. Sci. Lett.* 530.
- Jiang, G., Liu, L., Barbour, A.J., Lu, R., Yang, H., 2021. Physics-based evaluation of the maximum magnitude of potential earthquakes induced by the Hutubi (China) underground gas storage. *J. Geophys. Res. Solid Earth* 126.
- Li, J., Li, R., Wang, X., Shi, X., Qiao, X., Zheng, L., Abudutayier, Y., Sun, X., Chen, S., Fang, W., Cheng, R., 2016. Mechanism of surface vertical deformation in parts of the underground gas storage reservoir of Hutubi, Xinjiang, China. *Earthq. Res. China* 30, 451–463.
- Liu, G., Liao, W., Zhang, T., Zhao, Z., Chen, Y.e., Zhang, S., Sun, D., Rao, Y., 2019. Research on key technologies for dilatancy and recovery improving in Hutubi large-scale gas storage. *Sino-Glob. Energ.* 24, 46–53.
- Nikkhoo, M., Walter, T.R., Lundgren, P.R., Prats-Iraola, P., 2017. Compound dislocation models (CDMs) for volcano deformation analyses. *Geophys. J. Int.* 208, 877–894.
- Okada, Y., 1985. Surface deformation due to shear and tensile faults in a half-space. *Bull. Seismol. Soc. Am.* 75, 1135–1154.
- Okada, Y., 1992. Internal deformation due to shear and tensile faults in a half-space. *Bull. Seismol. Soc. Am.* 82, 1018–1040.
- Pang, J., Qian, G., Wang, B., Yang, Z., Wei, Y., Li, Y., 2012. Evaluation of sealing ability of underground gas storage converted from the Xinjiang H gas field. *Nat. Gas Ind.* 32, 83–85.
- Qiao, X., Chen, W., Wang, D., Nie, Z., Chen, Z., Li, J., Wang, X., Li, Y., Wang, T., Feng, G., 2018. Crustal deformation in the Hutubi underground gas storage site in China observed by GPS and InSAR measurements. *Seismol. Res. Lett.* 89, 1467–1477.
- Shirzaei, M., Ellsworth, W.L., Tiampo, K.F., Gonzalez, P.J., Manga, M., 2016. Surface uplift and time-dependent seismic hazard due to fluid injection in eastern Texas. *Science* 353, 1416–1419.
- Shirzaei, M., Manga, M., Zhai, G., 2019. Hydraulic properties of injection formations constrained by surface deformation. *Earth Planet. Sci. Lett.* 515, 125–134.
- Suckale, J., 2009. Induced seismicity in hydrocarbon fields. *Adv. Geophys.* 51, 55–106.
- Tang, L., Lu, Z., Zhang, M., Sun, L., Wen, L., 2018. Seismicity induced by simultaneous abrupt changes of injection rate and well pressure in Hutubi gas field. *J. Geophys. Res. Solid Earth* 123, 5929–5944.
- Teatini, P., Castelletto, N., Ferronato, M., Gambolati, G., Janna, C., Cairo, E., Marzorati, D., Colombo, D., Ferretti, A., Baglioni, A., Bottazzi, F., 2011. Geomechanical response to seasonal gas storage in depleted reservoirs: a case study in the Po River basin, Italy. *J. Geophys. Res. Earth Surf.* 116, F02002.
- Verdon, J.P., Kendall, J.M., Stork, A.L., Chadwick, R.A., White, D.J., Bissell, R.C., 2013. Comparison of geomechanical deformation induced by megatonne-scale CO₂ storage at Sleipner, Weyburn, and in Salah. *Proc. Natl. Acad. Sci. U. S. A.* 110, E2762–E2771.
- Werner, C., Wegmüller, U., Strozzi, T., Wiesmann, A., 2000. Gamma SAR and interferometric processing software. In: Proceedings of the Ers-envisat Symposium, Gothenburg, Sweden, 461, pp. 211–219.
- Werner, C., Wegmüller, U., Strozzi, T., Wiesmann, A., 2003. Interferometric point target analysis for deformation mapping. In: Igars 2003: Ieee International Geoscience and Remote Sensing Symposium, Vols I - VII, Proceedings, pp. 4362–4364.
- Xiong, Z., Feng, G., Feng, Z., Miao, L., Wang, Y., Yang, D., Luo, S., 2020. Pre- and post-failure spatial-temporal deformation pattern of the Baige landslide retrieved from multiple radar and optical satellite images. *Eng. Geol.* 279.
- Xu, W., Xie, L., Aoki, Y., Rivalta, E., Jónsson, S., 2020. Volcano-wide deformation after the 2017 Erta Ale Dike intrusion, Ethiopia, observed with radar interferometry. *J. Geophys. Res. Solid Earth* 125 e2020JB019562.
- Zebker, H.A., Rosen, P.A., Goldstein, R.M., Gabriel, A., Werner, C.L., 1994. On the derivation of coseismic displacement fields using differential radar interferometry: the landers earthquake. *J. Geophys. Res. Solid Earth* 99, 19617–19634.
- Zhou, P., Yang, H., Wang, B., Zhuang, J., 2019. Seismological investigations of induced earthquakes near the Hutubi underground gas storage facility. *J. Geophys. Res. Solid Earth* 124, 8753–8770.